
LPNSR: Optimal Noise-Guided Diffusion Image Super-Resolution Via Learnable Noise Prediction

Shuwei Huang, Shizhuo Liu, Zijun Wei

Huazhong University of Science and Technology

{frozen2001, shizhuo1}@hust.edu.cn, weiiizong1001@gmail.com

Abstract

Diffusion-based image super-resolution (SR) aims to reconstruct high-resolution (HR) images from low-resolution (LR) observations. However, the inherent randomness injected during the reverse diffusion process causes the performance of diffusion-based SR models to vary significantly across different sampling runs, particularly when the sampling trajectory is compressed into a limited number of steps. A critical yet underexplored question is: what is the optimal noise to inject at each intermediate diffusion step? In this paper, we establish a theoretical framework that derives the closed-form analytical solution for optimal intermediate noise in diffusion models from a maximum likelihood estimation perspective, revealing a consistent conditional dependence structure that generalizes across diffusion paradigms. We instantiate this framework under the residual-shifting diffusion paradigm and accordingly design an LR-guided multi-input-aware noise predictor to replace random Gaussian noise. We further mitigate initialization bias with a high-quality pre-upsampling network. The compact 4-step trajectory uniquely enables end-to-end optimization of the entire reverse chain, which is computationally prohibitive for conventional long-trajectory diffusion models. Extensive experiments demonstrate that LPNSR achieves state-of-the-art perceptual performance on both synthetic and real-world datasets, without relying on any large-scale text-to-image priors. The source code of our method can be found at <https://github.com/Faze-Hsw/LPNSR>.

1 Introduction

Image super-resolution (SR) aims to recover high-resolution (HR) images from low-resolution (LR) observations, a severely ill-posed problem due to unknown real-world degradations. Recently, diffusion models [1, 2, 3, 4, 5, 6, 7, 8, 9, 10] have demonstrated unprecedented potential in SR tasks, achieving remarkable breakthroughs in both pixel-level fidelity and perceptual realism. However, diffusion-based SR methods face a fundamental and critical trade-off between inference efficiency and reconstruction performance, especially in limited-step sampling scenarios that are essential for practical deployment.

To break this trade-off, the residual-shifting diffusion framework (ResShift [2]) has emerged as the state-of-the-art (SOTA) efficient solution, achieving SR inference with only 4 sampling steps while retaining a lightweight denoising network. However, due to sampling step compression, its 4-step version suffers from severe performance degradation compared to the 15-step counterpart. This performance decline exposes a fundamental flaw in mainstream diffusion pipelines [2, 11, 12, 13, 10]: the universal use of unconstrained random Gaussian noise in intermediate reverse steps. Existing attempts to address this issue mainly rely on distillation to compress the diffusion sampling trajectory into a single step [14, 8], which avoids introducing random Gaussian noise in intermediate steps, yet the performance is inherently bounded by the capacity of the teacher model. Diffusion inversion methods [15, 16, 17, 18, 19, 20] adopt step-wise optimization for intermediate noise.

However, existing diffusion inversion methods mainly focus on image editing and lack a closed-form definition of optimal noise with a generalizable structure across diffusion paradigms. In this work, we address these gaps by establishing a unified maximum likelihood estimation (MLE)-based theoretical framework to derive the closed-form analytical solution of optimal intermediate noise for diffusion models, revealing its consistent conditional dependence structure generalizable across mainstream diffusion paradigms, laying a theoretical foundation for mitigating few-step diffusion performance degradation.

We instantiate this framework on the residual-shifting diffusion paradigm, as its compact 4-step trajectory uniquely enables end-to-end optimization of the full reverse chain-computationally infeasible for long-trajectory models like DDPM [10]. This allows us to learn a deep neural network for the theoretically optimal noise without modifying the pretrained denoising network or breaking the original efficient residual-shifting mechanism. We further address initialization bias from bicubic upsampling, a critical bottleneck for few-step sampling where limited iterations cannot correct initial deviations, via a pretrained pre-upsampling network to generate a high-quality initial state before diffusion. An additional key benefit of this design is that it enables arbitrary-step super-resolution inference without redesigning the diffusion framework’s hyper parameters or retraining the pretrained denoising network.

Building on this, we propose LPNSR, an efficient prior-enhanced diffusion SR framework. It adopts an LR-guided multi-input-aware noise predictor (aligned with our derived optimal noise structure) to replace random Gaussian noise, paired with the pre-upsampling initialization strategy. Extensive experiments show LPNSR achieves state-of-the-art perceptual SR performance without external text-to-image (T2I) priors.

The main contributions of this work are as follows:

- We establish a unified MLE-based framework to derive the closed-form optimal intermediate noise for diffusion models, revealing its generalizable conditional dependence structure across paradigms.
- We instantiate this framework on the residual-shifting diffusion paradigm, designing an LR-guided noise predictor to approximate the optimal noise while fully preserving the original efficient inference mechanism.
- We mitigate few-step initialization bias via a pretrained pre-upsampling network, which significantly boosts compact-trajectory inference performance and enables flexible arbitrary-step inference without retraining the core denoising network.

2 Related work

Image Super-Resolution. Along with the proliferation of deep learning, deep learning-driven approaches have progressively emerged as the dominant paradigm for SR [21, 22]. Early prominent works primarily focused on training regression models using paired LR-HR data [23, 24, 25]. Though these models effectively capture the expectation of the posterior distribution, they inherently suffer from over-smoothing artifacts in generated results [26, 27, 28]. To enhance the perceptual quality of reconstructed HR images, generative SR models have garnered growing interest, including autoregressive architectures [29, 30, 31, 32]. Despite notable gains in perceptual performance, autoregressive models typically incur substantial computational overhead. Additionally, GAN-based SR methods have attained remarkable success in perceptual quality [33, 34, 26, 27, 28], yet the training process remains unstable. More recently, diffusion-based models have become a focal point of SR research [35, 6, 5, 7, 1]. These methods generally fall into two categories: those that concatenate the LR image to the denoiser’s input [7, 1], and those that adapt the backward process of a pre-trained diffusion model [35, 6, 5]. While these diffusion-based approaches yield promising performance, their methods still introduce unconstrained random Gaussian noise in each step of the reverse diffusion process, rather than meaningful noise maps.

Diffusion Inversion. This paradigm aims to find the optimal noise maps that reconstruct the target image when fed into a diffusion model. Early works optimized text embeddings for better alignment [36, 37], and follow-up works further refined inversion via textual/visual prompts [38, 39] or intermediate noise map optimization [40, 41, 42, 43]. However, existing diffusion inversion methods are mostly heuristic step-wise optimization schemes tailored for image editing tasks. None of them establish a unified, generalizable theoretical derivation paradigm for optimal intermediate

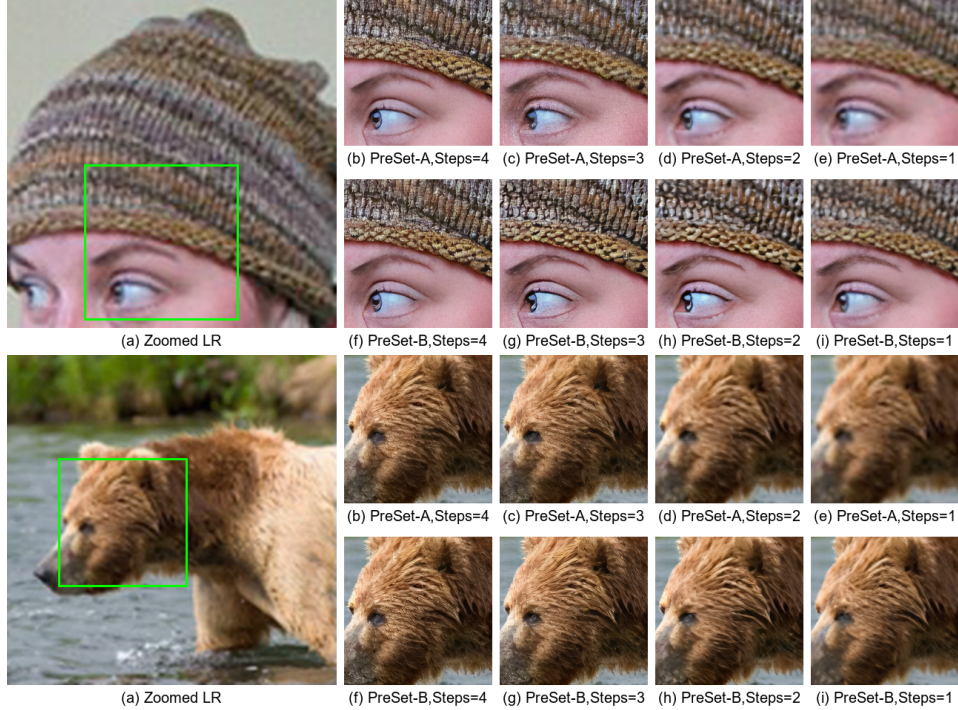


Figure 1: Qualitative comparison of our PreSet-A and PreSet-B methods under different sampling steps for $\times 4$ image super-resolution. (a) Zoomed patch of the input LR image; (b)-(e) Results of PreSet-A with 4, 3, 2, and 1 sampling steps, respectively; (f)-(i) Results of PreSet-B with 4, 3, 2, and 1 sampling steps, respectively. Two representative samples are provided to demonstrate the visual performance of different configurations. (Zoom in for best view)

noise, nor provide a closed-form analytical solution that can generalize across mainstream diffusion paradigms. For SR tasks, InvSR [4] extends diffusion inversion to SR, but it is constrained by the long sampling trajectory of DDPM [10], which makes full-chain end-to-end optimization computationally prohibitive. It only optimizes the initial noise map, and fails to solve the fundamental problem of defining and optimizing the optimal intermediate noise for the full reverse sampling chain.

3 Methodology

3.1 Preliminaries

We first establish a unified notation system for conditional diffusion models, which is generalizable to mainstream diffusion paradigms including DDPM [10] and residual-shifting framework [2], to lay a formal foundation for our theoretical derivation. We denote x_0 as the clean target sample (i.e., HR image in the SR task), and y as the task conditional input (i.e., the LR image in the SR task). The forward diffusion process is defined as a Markov chain of length T , which gradually corrupts the clean sample x_0 with noise. The single-step transition distribution follows an isotropic Gaussian distribution:

$$q(x_t|x_{t-1}, y) = \mathcal{N}\left(x_t; \mu_t^f(x_{t-1}, y), \Sigma_t^f \cdot \mathbf{I}\right), \quad t = 1, 2, \dots, T, \quad (1)$$

where $\mu_t^f(\cdot)$ and Σ_t^f are the forward transition mean function and scalar variance, specified by the target diffusion paradigm. For most mainstream paradigms, the forward process admits a closed-form marginal distribution, which directly gives the distribution of the noisy sample at arbitrary timestep t without iterative sampling:

$$q(x_t|x_0, y) = \mathcal{N}\left(x_t; \mu_t^m(x_0, y), \Sigma_t^m \cdot \mathbf{I}\right), \quad t = 1, 2, \dots, T, \quad (2)$$

where $\mu_t^m(\cdot)$ and Σ_t^m denoting the marginal mean function and scalar variance, respectively. The learnable reverse denoising process is an inverse Markov chain that reconstructs x_{t-1} from x_t under



Figure 2: Visualization of the intermediate noise maps generated by our proposed noise predictor during the 4-step reverse diffusion process. From left to right: the input LR image, and the predicted noise maps at step-4, step-3, and step-2 of the reverse sampling process, respectively.

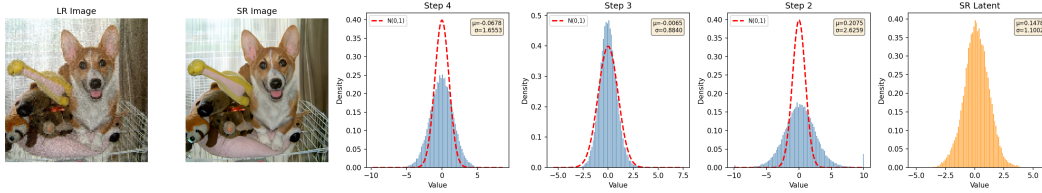


Figure 3: Statistical distribution analysis of the outputs from our LR-guided noise predictor. From left to right: the input LR image, the final SR image generated by LPNSR, the probability density distributions of the predicted noise maps at each intermediate reverse step ($t = 4$, $t = 3$, and $t = 2$), and the distribution of the final SR output in latent space. The mean (μ) and standard deviation (σ) of the noise/latent values are provided for each distribution.

the guidance of y , with Gaussian distribution:

$$p_{\theta}(x_{t-1}|x_t, y) = \mathcal{N}(x_{t-1}; \boldsymbol{\mu}_t^{\theta}(x_t, y, t), \Sigma_t \cdot \mathbf{I}), \quad (3)$$

where $\boldsymbol{\mu}_t^{\theta}(\cdot)$ is the reverse mean parameterized by a learnable denoising network f_{θ} , and Σ_t is the fixed or predefined reverse scalar variance. This gives the unified single-step reverse iteration:

$$x_{t-1} = \boldsymbol{\mu}_t^{\theta}(x_t, y, t) + \sqrt{\Sigma_t} \cdot z_{t-1}, \quad (4)$$

where z_{t-1} is the intermediate noise injected at step t , universally sampled from an unconstrained standard Gaussian distribution $\mathcal{N}(\mathbf{0}, \mathbf{I})$ in conventional pipelines, which is the core variable we optimize in this work.

3.2 Theoretical derivation of optimal intermediate noise

We define the optimal intermediate noise z_{t-1}^* as the noise that maximizes the conditional log-likelihood of the ground-truth x_0 given the intermediate state x_t and conditional input y , following the MLE paradigm for generative model optimization:

$$z_{t-1}^* = \arg \max_{z_{t-1}} \log p_{\theta}(x_0|x_{t-1}(z_{t-1}), y), \quad (5)$$

where $x_{t-1}(z_{t-1})$ is uniquely determined by z_{t-1} via Eq. (4). By Bayes' theorem, we decompose the posterior as

$$p_\theta(x_0|x_{t-1}, y) = \frac{q(x_{t-1}|x_0, y) \cdot p_\theta(x_0|y)}{p_\theta(x_{t-1}|y)}. \quad (6)$$

Following standard diffusion posterior derivation practices [44], the parameterized distribution $p_\theta(x_0|y)$ learned by a well-trained diffusion model is a fitting to the data probability distribution $q(x_0|y)$. Thus, we adopt a non-informative prior $p_\theta(x_0|y) \propto 1$, and the marginal likelihood $p_\theta(x_{t-1}|y)$ is a normalization constant independent of x_0 . This simplifies the posterior to $p_\theta(x_0|x_{t-1}, y) \propto q(x_{t-1}|x_0, y)$. Substituting the forward marginal Gaussian distribution in Eq. (2) and taking the logarithm, the log-likelihood becomes

$$\log p_\theta(x_0 | x_{t-1}, y) \propto -\frac{\|x_{t-1} - \boldsymbol{\mu}_{t-1}^m(x_0, y)\|^2}{2\Sigma_{t-1}^m}. \quad (7)$$

Maximizing the log-likelihood is equivalent to minimizing the above L2 norm, leading to the optimization objective:

$$z_{t-1}^* = \arg \min_{z_{t-1}} \|x_{t-1}(z_{t-1}) - \boldsymbol{\mu}_{t-1}^m(x_0, y)\|^2. \quad (8)$$

Substituting Eq. (4) into this objective and solving the convex optimization problem, we obtain the closed-form analytical solution of the optimal intermediate noise for general conditional diffusion models:

$$z_{t-1}^* = \frac{\boldsymbol{\mu}_{t-1}^m(x_0, y) - \boldsymbol{\mu}_t^\theta(x_t, y, t)}{\sqrt{\Sigma_t}}. \quad (9)$$

This closed-form solution yields three fundamental conclusions. First, the optimal intermediate noise is a deterministic mapping rather than an unconstrained random Gaussian variable, directly proving the inherent suboptimality of conventional random noise injection, especially in compact few-step sampling scenarios with severe error accumulation. Second, the optimal noise follows a unified conditional dependence structure across all mainstream diffusion paradigms, uniquely determined by the forward marginal mean $\boldsymbol{\mu}_{t-1}^m(x_0, y)$, reverse mean $\boldsymbol{\mu}_t^\theta(x_t, y, t)$, and reverse variance $\sqrt{\Sigma_t}$. Third, the solution explicitly defines the input variables required to approximate the optimal noise, providing theoretical guidance for the design of our noise prediction network.

3.3 Instantiation to residual-shifting diffusion SR paradigm

We instantiate our general optimal noise derivation paradigm proposed in Sec. 3.2 to the residual-shifting diffusion framework [2], an efficient SR pipeline with a compact 4-step sampling trajectory. Unlike long-trajectory models (e.g., DDPM [10]) requiring hundreds of steps, this 4-step design uniquely enables end-to-end optimization of the full reverse chain, which is computationally prohibitive for conventional long-trajectory diffusion models.

Optimal Intermediate Noise. We follow the native notation of the residual-shifting paradigm: y_0 is the input LR image, x_0 is the target HR image, and $e_0 = y_0 - x_0$ is the LR-HR residual. It's assumed that the input LR image y_0 shares the identical spatial dimension with the target HR image x_0 , which can be achieved by upsampling the raw LR input. Its forward marginal distribution are

$$q(x_t|x_0, y_0) = \mathcal{N}\left(x_t; \underbrace{(1 - \eta_t)x_0 + \eta_t y_0}_{\boldsymbol{\mu}_t^m(x_0, y_0)}, \underbrace{\kappa^2 \eta_t}_{\Sigma_t^m} \cdot \mathbf{I}\right), \quad (10)$$

where $\{\eta_t\}_{t=1}^T$ is a monotonically increasing shifting sequence ($\eta_1 \rightarrow 0, \eta_T \rightarrow 1$), κ is the noise variance hyperparameter. And its reverse process can be given as

$$p_\theta(x_{t-1}|x_t, y_0) = \mathcal{N}\left(x_{t-1}; \underbrace{\frac{\eta_{t-1}}{\eta_t} x_t + \frac{\alpha_t}{\eta_t} f_\theta(x_t, y_0, t)}_{\boldsymbol{\mu}_t^\theta(x_t, y_0, t)}, \underbrace{\kappa^2 \frac{\eta_{t-1} \alpha_t}{\eta_t}}_{\Sigma_t} \cdot \mathbf{I}\right), \quad (11)$$

where $\alpha_t = \eta_t - \eta_{t-1}$ ($\alpha_1 = \eta_1$), f_θ is the pretrained denoiser predicting clean image x_0 . Substituting the above marginal mean, reverse mean and variance into our general optimal noise solution Eq. (9), we directly obtain the closed-form optimal noise for this paradigm:

$$z_{t-1}^* = \frac{(1 - \eta_{t-1})x_0 + \eta_{t-1}y_0 - \boldsymbol{\mu}_t^\theta(x_t, y_0, t)}{\sqrt{\boldsymbol{\Sigma}_t}}. \quad (12)$$

This solution proves the inherent suboptimality of the original random Gaussian noise injection, and explicitly defines that the optimal noise is uniquely determined by $\{x_t, x'_0 = f_\theta(x_t, y_0, t), y_0, t\}$, providing theoretical guidance for our noise predictor design.

Initialization Strategy. For the residual-shifting paradigm, the forward marginal distribution at $t = T$ converges to $q(x_T|x_0, y_0) = \mathcal{N}(y_0, \kappa^2 \mathbf{I})$. During inference, the ground-truth x_0 is inaccessible, so we directly replace x_0 in the forward marginal distribution $q(x_t|x_0, y_0)$ with y_0 , yielding the arbitrary-step initialization formula:

$$x_t = y_0 + \kappa\sqrt{\eta_t} \cdot z_t, z_t \sim \mathcal{N}(\mathbf{0}, \mathbf{I}). \quad (13)$$

The validity of this approximation hinges on the proximity between y_0 and x_0 . The native pipeline uses naive bicubic upsampling to match y_0 to x_0 's dimension, but this fails to bring y_0 sufficiently close to ground-truth HR image x_0 , introducing severe initialization bias. In compact few-step trajectories, the model lacks enough iterations to correct this bias, causing dramatic performance degradation. We thus replace bicubic upsampling with a pretrained SwinIR-GAN [45] to generate dimension-matched y_0 , narrowing the $y_0 - x_0$ gap, mitigating initialization bias, boosting few-step performance, and enabling 1-4 step arbitrary inference without retraining the core denoiser (see Tab. 1).

End-to-End Optimization. Since x_0 is unavailable during inference, we adopt the UNet [46] used in [2] as the noise predictor g_ω to approximate the optimal noise in Eq. (12), taking $\{x_t, x'_0, y_0, t\}$ as input. The revised reverse iteration is

$$x_{t-1} = \boldsymbol{\mu}_t^\theta(x_t, y_0, t) + \sqrt{\boldsymbol{\Sigma}_t} \cdot g_\omega(x_t, x'_0, y_0, t). \quad (14)$$

Substituting the optimal noise into the reverse process (Eq. (11)) gives x_{t-1} that exactly matches the conditional mean of the forward marginal distribution (Eq. (10)), meaning injecting optimal noise at every step enforces the reverse trajectory to align with the forward process, and guarantees exact recovery of the ground-truth HR image for a well-trained denoiser f_θ . To enable g_ω to learn this optimal mapping, we optimize it end-to-end over the full 4-step reverse chain (computationally feasible only for this compact trajectory), freezing the pretrained denoiser f_θ and the VQGAN autoencoder [47]. Following recent SR approaches [1, 4, 48], the training objective is a combination of L1 loss L_1 , LPIPS [49] loss L_l , and GAN [50] loss L_g :

$$\mathcal{L} = \lambda_1 L_1(x'_0, x_0) + \lambda_l L_l(x'_0, x_0) + \lambda_g L_g(x'_0, x_0), \quad (15)$$

where x'_0 is the final predicted clean image. λ_1 , λ_l , and λ_g are hyperparameters balancing the contributions of each loss component. The detailed training and inference procedure is provided in Alg. 1 and Alg. 2.

4 Experiments

In this section, we compare our method against some of the recent state-of-the-art diffusion-based SR approaches, analyze the effectiveness of our LR-guided noise predictor, and perform ablation studies to understand the contributions of different components in our model. Our experiments mainly focus on the $\times 4$ SR task.

4.1 Experimental setup

Training Details. We train the noise predictor on the LSDIR [52] dataset and the first 10k face images from the FFHQ [53] dataset for over 200k iterations, randomly cropping an image patch with a resolution of 256×256 from the source image and synthesizing the LR image using the pipeline of RealESRGAN [48] at each iteration. We adopt the AdamW [54] optimizer with a learning rate of 5×10^{-5} and a batch size of 16, while using the CosineAnnealing [55] scheduler with a minimum

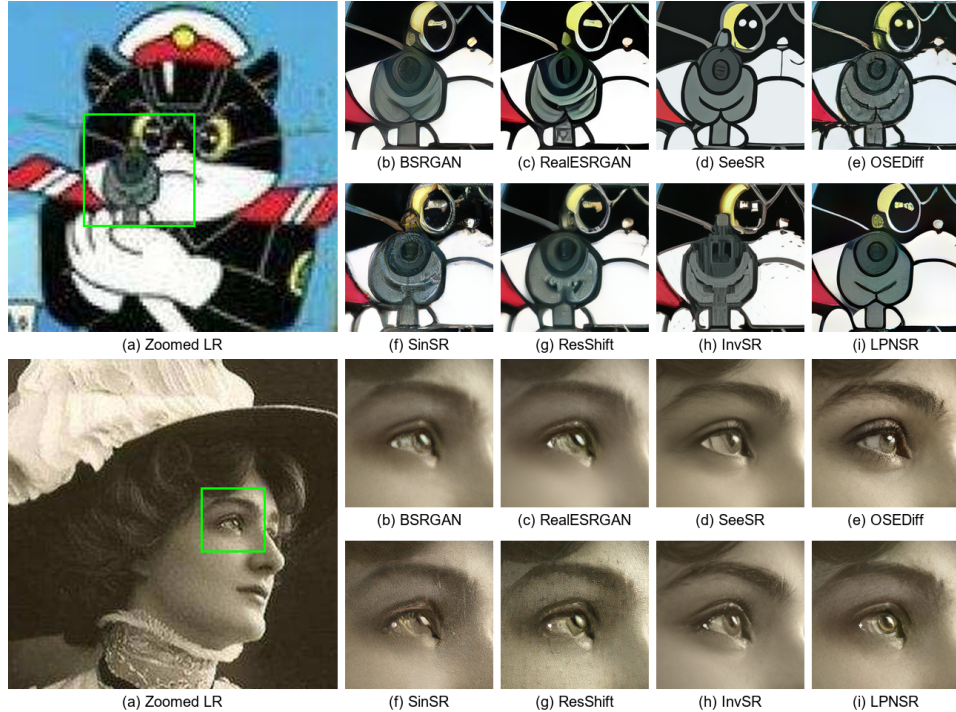


Figure 4: Visual results of different methods on two typical real-world examples. (Zoom in for best view)

learning rate of 1×10^{-5} . The hyperparameters for the loss function are set as $\lambda_1 = 1.0$, $\lambda_l = 1.0$, and $\lambda_g = 0.1$. During training, we set $T = 4$ to remain consistent with ResShift [2], and the noise variance hyperparameter $\kappa = 2.0$ as well as the shifting sequence $\{\eta_t\}_{t=1}^T$ also follow the identical settings. The denoising network f_θ and the VQGAN autoencoder [47] are frozen during training, only the noise predictor is optimized.

Testing Datasets and Metrics. To facilitate fair and direct comparison with the latest SOTA methods, we follow the experimental setup of InvSR [4] by adopting its testing datasets and evaluation metrics. Specifically, our experiments are conducted on the three datasets: the synthetic dataset ImageNet-Test [56] used in [4], the real-world datasets RealSR [57] and RealSet80 [2]. For evaluation metrics, we retain the same configuration: seven metrics (three reference metrics: PSNR, SSIM [58], LPIPS [49]; four non-reference metrics: NIQE [59], PI [60], MUSIQ [61], CLIPQA [62]) are employed for ImageNet-Test and RealSR, while only non-reference metrics are used for RealSet80. PSNR and SSIM are calculated on the luminance (Y) channel of YCbCr space, and other metrics are computed in the standard sRGB space.

Compared Methods. To benchmark our model, we compare it against eight recent methods: 2 GAN-based methods (BSRGAN [51], RealESRGAN [48]) and 5 diffusion-based methods (SeeSR [9], ResShift [2], SinSR [14], OSediff [8], InvSR [4]). The presets of all methods follow the official default guidelines.

4.2 Experimental results

Inference Steps. Tab. 1 compares our PreSet-A (noise predictor only) and PreSet-B (with pre-upsampling) methods against original ResShift [2] across 1-4 sampling steps. We observe that the pre-upsampling module delivers more significant gains with fewer steps, while our noise predictor stably improves perceptual performance across all settings, with all methods performing better with more steps. Regarding inference latency, our noise predictor introduces no noticeable overhead as its computation is performed entirely in the latent space. For 3-4 step inference, the model has sufficient iterations to mitigate initialization bias, so the pre-upsampling module can be optionally

Table 1: Quantitative comparison results between our proposed methods (denoted as PreSet-A, PreSet-B) and the original ResShift on the ImageNet-Test dataset, where PreSet-A uses only the noise predictor, and PreSet-B employs SwinIR-GAN to do pre-upsampling. The Runtime metric denotes the average inference time per image, which is tested on a single NVIDIA RTX 3090 Ti GPU. (Notably, the noise predictor is not activated during single-step inference, thus PreSet-A yields identical inference results to ResShift.)

Steps	Methods	Metrics							
		PSNR \uparrow	SSIM \uparrow	LPIPS \downarrow	NIQE \downarrow	PI \downarrow	CLIPQA \uparrow	MUSIQ \uparrow	Runtime(s)
$T = 1$	ResShift	28.96	0.7886	0.4183	7.7442	7.1397	0.2929	30.2567	0.64
	PreSet-A	28.96	0.7886	0.4183	7.7442	7.1397	0.2929	30.2567	0.64
	PreSet-B	27.11	0.7566	0.2185	5.2409	4.2176	0.5776	66.0646	0.81
$T = 2$	ResShift	28.48	0.7823	0.3335	7.1880	6.7002	0.3392	38.8335	0.69
	PreSet-A	28.01	0.7629	0.2861	5.9066	5.7823	0.3812	44.2488	0.71
	PreSet-B	25.94	0.7244	0.2214	4.2463	3.2883	0.6341	70.7036	0.89
$T = 3$	ResShift	28.62	0.7816	0.2487	6.1413	5.7854	0.4601	52.4232	0.74
	PreSet-A	26.68	0.7065	0.2561	4.4798	3.2974	0.6557	66.7649	0.77
	PreSet-B	25.99	0.7001	0.2575	4.4535	3.2303	0.6858	71.5964	0.98
$T = 4$	ResShift	27.33	0.7530	0.1998	5.8700	4.3643	0.6147	65.5860	0.81
	PreSet-A	26.35	0.7151	0.2324	4.4127	3.2834	0.6689	71.2560	0.90
	PreSet-B	26.11	0.7054	0.2424	4.3807	3.1995	0.6921	71.7105	1.09

Table 2: Quantitative comparisons of different methods on ImageNet-Test and RealSR datasets. The best and second-best results are highlighted in red and blue.

Datasets	Methods	Metrics						
		PSNR \uparrow	SSIM \uparrow	LPIPS \downarrow	NIQE \downarrow	PI \downarrow	CLIPQA \uparrow	MUSIQ \uparrow
<i>ImageNet-Test</i>	BSRGAN [51]	27.05	0.7453	0.2437	4.5345	3.7111	0.5703	67.7195
	RealESRGAN [48]	26.62	0.7523	0.2303	4.4909	3.7234	0.5090	64.8186
	SeeSR [9]	26.69	0.7422	0.2187	4.3825	3.4742	0.5868	71.2412
	ResShift [2]	27.33	0.7530	0.1998	5.8700	4.3643	0.6147	65.5860
	SinSR [14]	26.98	0.7304	0.2209	5.2623	3.8189	0.6618	67.7593
	OSDiff [8]	23.95	0.6756	0.2624	4.7157	3.3775	0.6818	70.3928
	InvSR [4]	24.14	0.6789	0.2517	4.3815	3.0866	0.7093	72.2900
	LPNSR(Ours)	26.11	0.7054	0.2424	4.3807	3.1995	0.6921	71.7105
<i>RealSR</i>	BSRGAN [51]	26.51	0.7746	0.2685	4.6501	4.4644	0.5439	63.5869
	RealESRGAN [48]	25.85	0.7734	0.2728	4.6766	4.4881	0.4898	59.6803
	SeeSR [9]	26.20	0.7555	0.2806	4.5358	4.1464	0.6824	66.3757
	ResShift [2]	25.77	0.7453	0.3395	6.9113	5.4013	0.5994	57.5536
	SinSR [14]	26.02	0.7097	0.3993	6.2547	4.7183	0.6634	59.2981
	OSDiff [8]	23.89	0.7030	0.3288	5.3310	4.3584	0.7008	65.4806
	InvSR [4]	24.50	0.7262	0.2872	4.2189	3.7779	0.6918	67.4586
	LPNSR(Ours)	24.62	0.7003	0.3229	4.2175	3.6963	0.7180	67.5634

excluded to trade off a minor performance drop for faster inference. For 1-2 step inference, however, the pre-upsampling module is indispensable, as the limited sampling steps cannot compensate for initialization deviation without high-quality pre-upsampling. Qualitative results in Fig. 1 confirm that PreSet-B maintains consistent visual quality even in 1-2 step inference, while PreSet-A suffers from blurriness in low-step settings. We fix 4-step inference with pre-upsampling as our default LPNSR configuration for all following experiments.

Performance Comparison. Tab. 2 and 3 present a comprehensive comparison of our LPNSR against recent SOTA methods on the ImageNet-Test, RealSR and RealSet80 datasets. Compared to the baseline ResShift [2], our LPNSR achieves remarkable improvements in perceptual metrics (e.g., NIQE, CLIPQA, MUSIQ) while maintaining competitive fidelity. Against T2I-utilizing models such as OSDiff [8], InvSR [4] and SeeSR [9], LPNSR delivers comparable or better perceptual quality without leveraging any pre-trained text-to-image priors. It also outperforms multi-step diffusion methods (e.g., SeeSR [9]) on core perceptual metrics. On real-world datasets, LPNSR ranks among

Table 3: Quantitative comparisons of various methods on RealSet80 dataset. The best and second-best results are highlighted in red and blue.

Method	NIQE↓	PI↓	CLIQQA↑	MUSIQ↑
BSRGAN [51]	4.4408	4.0276	0.6263	66.6288
RealESRGAN [48]	4.1568	3.8852	0.6189	64.4957
SeeSR [9]	4.3678	3.7429	0.7114	69.7658
ResShift [2]	5.9866	4.8318	0.6515	61.7967
SinSR [14]	5.6243	4.2830	0.7228	64.0573
OSDiff [8]	4.3457	3.8219	0.7093	68.8202
InvSR [4]	4.0284	3.4666	0.7291	69.8055
LPNSR(Ours)	4.3066	3.5845	0.7316	70.2184

Table 4: Ablation study results of noise predictor at each intermediate step on the RealSR dataset. We evaluate the performance of LPNSR when replacing the noise predictor with random Gaussian noise at $t = 4$, $t = 3$, and $t = 2$ individually, under the 4-step sampling setting.

Method	PSNR↑	SSIM↑	LPIPS↓	NIQE↓	PI↓	CLIQQA↑	MUSIQ↑
LPNSR w/o Predictor at $t = 4$	24.53	0.6898	0.3434	4.3864	3.7770	0.7090	66.7373
LPNSR w/o Predictor at $t = 3$	24.05	0.6848	0.3404	4.3860	3.7553	0.7374	67.3563
LPNSR w/o Predictor at $t = 2$	24.86	0.7308	0.3117	5.8530	4.7332	0.7041	63.5838
LPNSR	24.62	0.7003	0.3229	4.2175	3.6963	0.7180	67.5634

the top-tier SOTA methods. It achieves leading perception-oriented metrics, such as NIQE, PI, CLIQQA and MUSIQ on RealSR. On RealSet80, LPNSR attains top-2 PI score, the best MUSIQ and CLIQQA scores among all competing methods. Qualitatively, Fig. 4 shows LPNSR generates sharper textures and more consistent structures than other methods, free from spurious details or over-smoothing (see Appendix for more visual comparisons). LPNSR generates SR images with sharp details, intact structural consistency, and no noticeable artifacts. It effectively restores natural textures and clear edge contours that align with the input LR structure, delivering visually coherent and realistic results.

Analysis and Ablation Study of Noise Predictor. Across the 4-step coarse-to-fine denoising trajectory, our LR-guided noise predictor implements progressive prior guidance aligned with the denoising logic. As shown in Fig. 2, the predicted noise maps are highly aligned with the LR image’s structure and texture, following a hierarchical guidance pattern: the step 4 map anchors global structure to avoid initial sampling deviation, the step 3 map focuses on mid-frequency texture refinement to suppress cumulative error, and the step 2 map targets local fine-grained details to optimize perceptual quality. Statistical distribution analysis in Fig. 3 further confirms that the optimized noise distributions at all steps are not unconstrained random Gaussian distributions. We further conduct a step-wise ablation study on the RealSR dataset (see Tab. 4) to quantitatively verify the independent contribution of each step’s predictor: the full LPNSR model achieves the best overall performance, validating the effectiveness of our full-stage prior guidance; removing the step 4 predictor degrades both fidelity and perceptual quality, disabling the step 3 predictor causes the most severe PSNR drop, and replacing the step 2 predictor with random noise sharply impairs perceptual metrics, fully consistent with our qualitative and statistical observations.

5 Conclusion

In this paper, we propose LPNSR, an efficient prior-enhanced diffusion SR framework. We first establish a unified MLE-based theoretical framework to derive the closed-form optimal intermediate noise for general diffusion models, and instantiate it to the residual-shifting diffusion paradigm with an LR-guided noise predictor and high-quality pre-upsampling initialization. Extensive experiments show that our 4-step LPNSR achieves SOTA perceptual performance on both synthetic and real-world datasets without external text-to-image priors, and supports flexible 1-4 step arbitrary inference. The core optimal noise derivation paradigm can be generalized to other diffusion frameworks, and we leave efficient training schemes for long-trajectory models to future work.

References

- [1] Chitwan Saharia, Jonathan Ho, William Chan, Tim Salimans, David J. Fleet, and Mohammad Norouzi. Image super-resolution via iterative refinement. *IEEE Transactions on Pattern Analysis and Machine Intelligence*, 45(4):4713–4726, 2023.
- [2] Zongsheng Yue, Jianyi Wang, and Chen Change Loy. Resshift: Efficient diffusion model for image super-resolution by residual shifting. In A. Oh, T. Naumann, A. Globerson, K. Saenko, M. Hardt, and S. Levine, editors, *Advances in Neural Information Processing Systems*, volume 36, pages 13294–13307. Curran Associates, Inc., 2023.
- [3] Jianyi Wang, Zongsheng Yue, Shangchen Zhou, Kelvin CK Chan, and Chen Change Loy. Exploiting diffusion prior for real-world image super-resolution. *International Journal of Computer Vision*, 132(12):5929–5949, 2024.
- [4] Zongsheng Yue, Kang Liao, and Chen Change Loy. Arbitrary-steps image super-resolution via diffusion inversion. In *Proceedings of the IEEE/CVF Conference on Computer Vision and Pattern Recognition (CVPR)*, pages 23153–23163, June 2025.
- [5] Bahjat Kawar, Michael Elad, Stefano Ermon, and Jiaming Song. Denoising diffusion restoration models. In S. Koyejo, S. Mohamed, A. Agarwal, D. Belgrave, K. Cho, and A. Oh, editors, *Advances in Neural Information Processing Systems*, volume 35, pages 23593–23606. Curran Associates, Inc., 2022.
- [6] Hyungjin Chung, Byeongsu Sim, and Jong Chul Ye. Come-closer-diffuse-faster: Accelerating conditional diffusion models for inverse problems through stochastic contraction. In *Proceedings of the IEEE/CVF Conference on Computer Vision and Pattern Recognition (CVPR)*, pages 12413–12422, June 2022.
- [7] Robin Rombach, Andreas Blattmann, Dominik Lorenz, Patrick Esser, and Björn Ommer. High-resolution image synthesis with latent diffusion models. In *Proceedings of the IEEE/CVF Conference on Computer Vision and Pattern Recognition (CVPR)*, pages 10684–10695, June 2022.
- [8] Rongyuan Wu, Lingchen Sun, Zhiyuan Ma, and Lei Zhang. One-step effective diffusion network for real-world image super-resolution. *Advances in Neural Information Processing Systems*, 37:92529–92553, 2024.
- [9] Rongyuan Wu, Tao Yang, Lingchen Sun, Zhengqiang Zhang, Shuai Li, and Lei Zhang. Seesr: Towards semantics-aware real-world image super-resolution. In *Proceedings of the IEEE/CVF conference on computer vision and pattern recognition*, pages 25456–25467, 2024.
- [10] Jonathan Ho, Ajay Jain, and Pieter Abbeel. Denoising diffusion probabilistic models. In H. Larochelle, M. Ranzato, R. Hadsell, M.F. Balcan, and H. Lin, editors, *Advances in Neural Information Processing Systems*, volume 33, pages 6840–6851. Curran Associates, Inc., 2020.
- [11] Cheng Lu, Yuhao Zhou, Fan Bao, Jianfei Chen, Chongxuan Li, and Jun Zhu. Dpm-solver: A fast ode solver for diffusion probabilistic model sampling in around 10 steps. *Advances in neural information processing systems*, 35:5775–5787, 2022.
- [12] Alexander Quinn Nichol and Prafulla Dhariwal. Improved denoising diffusion probabilistic models. In *International conference on machine learning*, pages 8162–8171. PMLR, 2021.
- [13] Jiaming Song, Chenlin Meng, and Stefano Ermon. Denoising diffusion implicit models. *arXiv preprint arXiv:2010.02502*, 2020.
- [14] Yufei Wang, Wenhan Yang, Xinyuan Chen, Yaohui Wang, Lanqing Guo, Lap-Pui Chau, Ziwei Liu, Yu Qiao, Alex C Kot, and Bihan Wen. Sinsr: diffusion-based image super-resolution in a single step. In *Proceedings of the IEEE/CVF conference on computer vision and pattern recognition*, pages 25796–25805, 2024.
- [15] Hyungjin Chung, Byeongsu Sim, Dohoon Ryu, and Jong Chul Ye. Improving diffusion models for inverse problems using manifold constraints. *Advances in Neural Information Processing Systems*, 35:25683–25696, 2022.
- [16] Hyungjin Chung, Jeongsol Kim, Michael T Mccann, Marc L Klasky, and Jong Chul Ye. Diffusion posterior sampling for general noisy inverse problems. *arXiv preprint arXiv:2209.14687*, 2022.
- [17] Ben Fei, Zhaoyang Lyu, Liang Pan, Junzhe Zhang, Weidong Yang, Tianyue Luo, Bo Zhang, and Bo Dai. Generative diffusion prior for unified image restoration and enhancement. In *Proceedings of the IEEE/CVF conference on computer vision and pattern recognition*, pages 9935–9946, 2023.

- [18] Jiaming Song, Arash Vahdat, Morteza Mardani, and Jan Kautz. Pseudoinverse-guided diffusion models for inverse problems. In *International Conference on Learning Representations*, 2023.
- [19] Jie Xiao, Ruili Feng, Han Zhang, Zhiheng Liu, Zhantao Yang, Yurui Zhu, Xueyang Fu, Kai Zhu, Yu Liu, and Zheng-Jun Zha. Dreamclean: Restoring clean image using deep diffusion prior. In *The Twelfth International Conference on Learning Representations*, 2024.
- [20] Zongsheng Yue and Chen Change Loy. Difface: Blind face restoration with diffused error contraction. *IEEE Transactions on Pattern Analysis and Machine Intelligence*, 46(12):9991–10004, 2024.
- [21] Chao Dong, Chen Change Loy, Kaiming He, and Xiaoou Tang. Image super-resolution using deep convolutional networks. *IEEE transactions on pattern analysis and machine intelligence*, 38(2):295–307, 2015.
- [22] Pablo Rojas Sedó. Deep learning for image super resolution. B.S. thesis, Universitat Politècnica de Catalunya, 2022.
- [23] Namhyuk Ahn, Byungkon Kang, and Kyung-Ah Sohn. Image super-resolution via progressive cascading residual network. In *Proceedings of the IEEE Conference on Computer Vision and Pattern Recognition Workshops*, pages 791–799, 2018.
- [24] Jiwon Kim, Jung Kwon Lee, and Kyoung Mu Lee. Accurate image super-resolution using very deep convolutional networks. In *Proceedings of the IEEE conference on computer vision and pattern recognition*, pages 1646–1654, 2016.
- [25] Zhaowen Wang, Ding Liu, Jianchao Yang, Wei Han, and Thomas Huang. Deep networks for image super-resolution with sparse prior. In *Proceedings of the IEEE international conference on computer vision*, pages 370–378, 2015.
- [26] Christian Ledig, Lucas Theis, Ferenc Huszár, Jose Caballero, Andrew Cunningham, Alejandro Acosta, Andrew Aitken, Alykhan Tejani, Johannes Totz, Zehan Wang, et al. Photo-realistic single image super-resolution using a generative adversarial network. In *Proceedings of the IEEE conference on computer vision and pattern recognition*, pages 4681–4690, 2017.
- [27] Sachit Menon, Alexandru Damian, Shijia Hu, Nikhil Ravi, and Cynthia Rudin. Pulse: Self-supervised photo upsampling via latent space exploration of generative models. In *Proceedings of the IEEE/CVF conference on computer vision and pattern recognition*, pages 2437–2445, 2020.
- [28] Mehdi SM Sajjadi, Bernhard Scholkopf, and Michael Hirsch. Enhancenet: Single image super-resolution through automated texture synthesis. In *Proceedings of the IEEE international conference on computer vision*, pages 4491–4500, 2017.
- [29] Ryan Dahl, Mohammad Norouzi, and Jonathon Shlens. Pixel recursive super resolution. In *Proceedings of the IEEE international conference on computer vision*, pages 5439–5448, 2017.
- [30] Jacob Menick and Nal Kalchbrenner. Generating high fidelity images with subscale pixel networks and multidimensional upscaling. *arXiv preprint arXiv:1812.01608*, 2018.
- [31] Aaron Van den Oord, Nal Kalchbrenner, Lasse Espeholt, Oriol Vinyals, Alex Graves, et al. Conditional image generation with pixelcnn decoders. *Advances in neural information processing systems*, 29, 2016.
- [32] Niki Parmar, Ashish Vaswani, Jakob Uszkoreit, Lukasz Kaiser, Noam Shazeer, Alexander Ku, and Dustin Tran. Image transformer. In *International conference on machine learning*, pages 4055–4064. PMLR, 2018.
- [33] Baisong Guo, Xiaoyun Zhang, Haoning Wu, Yu Wang, Ya Zhang, and Yan-Feng Wang. Lar-sr: A local autoregressive model for image super-resolution. In *Proceedings of the IEEE/CVF conference on computer vision and pattern recognition*, pages 1909–1918, 2022.
- [34] Tero Karras, Timo Aila, Samuli Laine, and Jaakko Lehtinen. Progressive growing of gans for improved quality, stability, and variation. *arXiv preprint arXiv:1710.10196*, 2017.
- [35] Jooyoung Choi, Sungwon Kim, Yonghyun Jeong, Youngjune Gwon, and Sungroh Yoon. Ilvr: Conditioning method for denoising diffusion probabilistic models. *arXiv preprint arXiv:2108.02938*, 2021.
- [36] Rinon Gal, Yuval Alaluf, Yuval Atzmon, Or Patashnik, Amit H Bermano, Gal Chechik, and Daniel Cohen-Or. An image is worth one word: Personalizing text-to-image generation using textual inversion. *arXiv preprint arXiv:2208.01618*, 2022.

- [37] Ron Mokady, Amir Hertz, Kfir Aberman, Yael Pritch, and Daniel Cohen-Or. Null-text inversion for editing real images using guided diffusion models. In *Proceedings of the IEEE/CVF conference on computer vision and pattern recognition*, pages 6038–6047, 2023.
- [38] Daiki Miyake, Akihiro Iohara, Yu Saito, and Toshiyuki Tanaka. Negative-prompt inversion: Fast image inversion for editing with text-guided diffusion models. In *2025 IEEE/CVF Winter Conference on Applications of Computer Vision (WACV)*, pages 2063–2072. IEEE, 2025.
- [39] Thao Nguyen, Yuheng Li, Utkarsh Ojha, and Yong Jae Lee. Visual instruction inversion: Image editing via image prompting. *Advances in Neural Information Processing Systems*, 36:9598–9613, 2023.
- [40] Xuan Ju, Ailing Zeng, Yuxuan Bian, Shaoteng Liu, and Qiang Xu. Direct inversion: Boosting diffusion-based editing with 3 lines of code. *arXiv preprint arXiv:2310.01506*, 2023.
- [41] Wonjun Kang, Kevin Galim, and Hyung Il Koo. Eta inversion: Designing an optimal eta function for diffusion-based real image editing. In *European Conference on Computer Vision*, pages 90–106. Springer, 2024.
- [42] Barak Meiri, Dvir Samuel, Nir Darshan, Gal Chechik, Shai Avidan, and Rami Ben-Ari. Fixed-point inversion for text-to-image diffusion models. *CoRR*, 2023.
- [43] Bram Wallace, Akash Gokul, and Nikhil Naik. Edict: Exact diffusion inversion via coupled transformations. In *Proceedings of the IEEE/CVF Conference on Computer Vision and Pattern Recognition*, pages 22532–22541, 2023.
- [44] Yiyang Ma, Huan Yang, Wenhan Yang, Jianlong Fu, and Jiaying Liu. Solving diffusion odes with optimal boundary conditions for better image super-resolution. *arXiv preprint arXiv:2305.15357*, 2023.
- [45] Jingyun Liang, Jiezhong Cao, Guolei Sun, Kai Zhang, Luc Van Gool, and Radu Timofte. Swinir: Image restoration using swin transformer. In *Proceedings of the IEEE/CVF international conference on computer vision*, pages 1833–1844, 2021.
- [46] Olaf Ronneberger, Philipp Fischer, and Thomas Brox. U-net: Convolutional networks for biomedical image segmentation. In *International Conference on Medical image computing and computer-assisted intervention*, pages 234–241. Springer, 2015.
- [47] Patrick Esser, Robin Rombach, and Bjorn Ommer. Taming transformers for high-resolution image synthesis. In *Proceedings of the IEEE/CVF Conference on Computer Vision and Pattern Recognition (CVPR)*, pages 12873–12883, June 2021.
- [48] Xintao Wang, Liangbin Xie, Chao Dong, and Ying Shan. Real-esrgan: Training real-world blind super-resolution with pure synthetic data. In *Proceedings of the IEEE/CVF international conference on computer vision*, pages 1905–1914, 2021.
- [49] Richard Zhang, Phillip Isola, Alexei A Efros, Eli Shechtman, and Oliver Wang. The unreasonable effectiveness of deep features as a perceptual metric. In *Proceedings of the IEEE conference on computer vision and pattern recognition*, pages 586–595, 2018.
- [50] Ian Goodfellow, Jean Pouget-Abadie, Mehdi Mirza, Bing Xu, David Warde-Farley, Sherjil Ozair, Aaron Courville, and Yoshua Bengio. Generative adversarial nets. In *Advances in Neural Information Processing Systems*, pages 2672–2680, 2014.
- [51] Kai Zhang, Jingyun Liang, Luc Van Gool, and Radu Timofte. Designing a practical degradation model for deep blind image super-resolution. In *Proceedings of the IEEE/CVF international conference on computer vision*, pages 4791–4800, 2021.
- [52] Yawei Li, Kai Zhang, Jingyun Liang, Jiezhong Cao, Ce Liu, Rui Gong, Yulun Zhang, Hao Tang, Yun Liu, Denis Demandolx, et al. Lsdir: A large scale dataset for image restoration. In *Proceedings of the IEEE/CVF Conference on Computer Vision and Pattern Recognition*, pages 1775–1787, 2023.
- [53] Tero Karras, Samuli Laine, and Timo Aila. A style-based generator architecture for generative adversarial networks. In *Proceedings of the IEEE/CVF conference on computer vision and pattern recognition*, pages 4401–4410, 2019.
- [54] Ilya Loshchilov and Frank Hutter. Decoupled weight decay regularization. *arXiv preprint arXiv:1711.05101*, 2017.
- [55] Ilya Loshchilov and Frank Hutter. Sgdr: Stochastic gradient descent with warm restarts. *arXiv preprint arXiv:1608.03983*, 2016.

- [56] Jia Deng, Wei Dong, Richard Socher, Li-Jia Li, Kai Li, and Li Fei-Fei. Imagenet: A large-scale hierarchical image database. In *2009 IEEE conference on computer vision and pattern recognition*, pages 248–255. Ieee, 2009.
- [57] Jianrui Cai, Hui Zeng, Hongwei Yong, Zisheng Cao, and Lei Zhang. Toward real-world single image super-resolution: A new benchmark and a new model. In *Proceedings of the IEEE/CVF international conference on computer vision*, pages 3086–3095, 2019.
- [58] Zhou Wang, Alan C Bovik, Hamid R Sheikh, and Eero P Simoncelli. Image quality assessment: from error visibility to structural similarity. *IEEE transactions on image processing*, 13(4):600–612, 2004.
- [59] Anish Mittal, Rajiv Soundararajan, and Alan C Bovik. Making a “completely blind” image quality analyzer. *IEEE Signal processing letters*, 20(3):209–212, 2012.
- [60] Yochai Blau, Roey Mechrez, Radu Timofte, Tomer Michaeli, and Lihi Zelnik-Manor. The 2018 pirm challenge on perceptual image super-resolution. In *Proceedings of the European conference on computer vision (ECCV) workshops*, pages 0–0, 2018.
- [61] Junjie Ke, Qifei Wang, Yilin Wang, Peyman Milanfar, and Feng Yang. Musiq: Multi-scale image quality transformer. In *Proceedings of the IEEE/CVF international conference on computer vision*, pages 5148–5157, 2021.
- [62] Jianyi Wang, Kelvin CK Chan, and Chen Change Loy. Exploring clip for assessing the look and feel of images. In *Proceedings of the AAAI conference on artificial intelligence*, volume 37, pages 2555–2563, 2023.

A Appendix

In the appendix, we provide the following materials:

- Extension to the DDPM Paradigm
- Quantitative and qualitative results of different noise injection strategies.
- Ablation study on the loss function.
- Different pre-upsampling backbones for the 4-step diffusion SR.
- More qualitative comparisons with state-of-the-art methods.
- The complete training and inference algorithms of our LPNSR framework.

A.1 Extension of optimal intermediate noise derivation to the DDPM paradigm

In this section, we extend the unified maximum likelihood estimation (MLE)-based optimal intermediate noise derivation framework from the main paper to the DDPM paradigm [10], following the unified notation system for conditional diffusion models established in the main paper. For the conditional DDPM framework, we follow its native notation: let $\beta_t \in (0, 1)$ be the predefined noise schedule, with $\alpha_t = 1 - \beta_t$ and $\bar{\alpha}_t = \prod_{s=1}^t \alpha_s$ as the cumulative product of α_t . The forward diffusion process corrupts x_0 with Gaussian noise, with a closed-form marginal distribution at timestep t :

$$q(x_t|x_0, y_0) = \mathcal{N}(x_t; \sqrt{\bar{\alpha}_t}x_0, (1 - \bar{\alpha}_t) \cdot \mathbf{I}), \quad (16)$$

with corresponding forward marginal mean $\mu_t^m(x_0, y_0) = \sqrt{\bar{\alpha}_t}x_0$ and marginal variance $\sum_t^m = 1 - \bar{\alpha}_t$. For the DDPM reverse denoising process, the single-step transition follows an isotropic Gaussian distribution, with the reverse mean parameterized by the denoising network ϵ_θ :

$$\mu_t^\theta(x_t, y_0, t) = \frac{1}{\sqrt{\alpha_t}} \left(x_t - \frac{1 - \alpha_t}{\sqrt{1 - \bar{\alpha}_t}} \epsilon_\theta(x_t, y_0, t) \right). \quad (17)$$

The reverse variance σ_t^2 follows the original DDPM fixed setting, corresponding to $\sqrt{\sum_t} = \sigma_t$ in our unified notation, with the reverse iteration given by $x_{t-1} = \mu_t^\theta(x_t, y_0, t) + \sigma_t \cdot z_{t-1}$, where z_{t-1} is the intermediate noise universally sampled from a standard Gaussian distribution in conventional DDPM pipelines. Substituting the DDPM formulation into our general optimal noise solution in Eq. (9), we directly obtain the closed-form optimal intermediate noise for the DDPM paradigm:

$$z_{t-1}^* = \frac{\sqrt{\bar{\alpha}_{t-1}}x_0 - \frac{1}{\sqrt{\alpha_t}} \left(x_t - \frac{1 - \alpha_t}{\sqrt{1 - \bar{\alpha}_t}} \epsilon_\theta(x_t, y_0, t) \right)}{\sigma_t}. \quad (18)$$

This result aligns perfectly with the core conclusions of the main paper, proving that the optimal intermediate noise for DDPM is a deterministic mapping rather than unconstrained random Gaussian noise, verifying that our MLE-based derivation framework is generalizable across mainstream diffusion paradigms beyond the residual-shifting framework, and provides theoretical guidance for optimal noise design in long-trajectory DDPM-based SR models.

A.2 Validation of SR-Based approximate optimal noise

In this section, we verify the feasibility of generating approximate optimal noise via a SR image as a proxy for the ground-truth HR image. Specifically, we use the pre-upsampled output of SwinIR-GAN [45] as the x_0 substitute in Eq. (12) to generate noise, and perform the full 4-step inference to produce the final result. We compare its performance with that of random Gaussian noise, theoretical optimal noise (calculated from the ground-truth HR image), and our LR-guided noise predictor, with results presented in Tab. 5. It can be seen that the theoretical optimal noise achieves perfect pixel-level reconstruction of the ground-truth HR image, and the approximate optimal noise significantly improves reconstruction fidelity, while its perceptual quality is inferior to our trained noise predictor. Fig. 5 presents the qualitative comparison of all noise injection strategies. Our LR-guided noise predictor produces results that closely align with the theoretical optimal noise, faithfully recovering fine details and structures consistent with the LR input. In comparison, the approximate optimal noise shows limited perceptual quality, while unconstrained random Gaussian noise results in severe misalignment between the generated textures and structures and the input LR image.

Table 5: Quantitative comparison of different intermediate noise injection strategies on ImageNet-Test and RealSR datasets.

Dataset	Noise Injection Strategy	PSNR \uparrow	SSIM \uparrow	LPIPS \downarrow	NIQE \downarrow	PI \downarrow	CLIPQA \uparrow	MUSIQ \uparrow
<i>ImageNet-Test</i>	Random Gaussian Noise	24.70	0.6567	0.3043	6.8422	4.4138	0.7341	70.8225
	Approximate Optimal Noise	27.46	0.7636	0.2242	5.3760	4.3798	0.5679	66.2120
	LR-Guided Noise Predictor	26.11	0.7054	0.2424	4.3807	3.1995	0.6921	71.7105
	Theoretical Optimal Noise	34.61	0.9282	0.0452	5.1169	4.1068	0.5623	65.3368
<i>RealSR</i>	Random Gaussian Noise	22.68	0.6194	0.4160	6.9618	5.1249	0.7162	60.9120
	Approximate Optimal Noise	27.02	0.7942	0.2597	5.4754	5.3232	0.4993	60.0818
	LR-Guided Noise Predictor	24.62	0.7003	0.3229	4.2175	3.6963	0.7180	67.5634
	Theoretical Optimal Noise	35.83	0.9723	0.0338	6.0362	5.5348	0.4684	58.6619

Table 6: Quantitative ablation studies on the loss function, wherein the hyper-parameters λ_l and λ_g control the weight importance of the LPIPS loss and the GAN loss, respectively. The results are evaluated on the ImageNet-Test dataset under the 4-step sampling setting.

Methods	Hyper-parameters		Metrics						
	λ_l (LPIPS loss)	λ_g (GAN loss)	PSNR \uparrow	SSIM \uparrow	LPIPS \downarrow	NIQE \downarrow	PI \downarrow	CLIPQA \uparrow	MUSIQ \uparrow
Baseline1	0.0	0.0	27.20	0.7265	0.2823	5.2234	3.8354	0.6268	66.6248
Baseline2	1.0	0.0	26.70	0.7158	0.2643	4.7588	3.5213	0.6621	69.5726
Baseline3	0.0	0.1	25.95	0.7003	0.2513	4.4315	3.2229	0.7044	72.1065
LPNSR	1.0	0.1	26.11	0.7054	0.2424	4.3807	3.1995	0.6921	71.7105

A.3 Ablation study on the loss functions

Tab. 6 presents the ablation results of our loss function on the ImageNet-Test dataset. The L1 loss alone ensures optimal pixel fidelity but leads to poor perceptual quality; the LPIPS loss balances fidelity and visual similarity, while the GAN loss significantly enhances image realism. Our final combined loss achieves the best trade-off between pixel-level fidelity and perceptual realism, which is the core reason for adopting this configuration in our study.

A.4 Pre-Upsampling backbones

We evaluate the performance of our 4-step diffusion SR framework equipped with different pre-upsampling backbones, with quantitative results presented in Tab. 7. All three tested networks (BSRGAN [51], RealESRGAN [48], SwinIR-GAN [45]) deliver comparable fidelity performance on both ImageNet-Test and RealSR datasets, verifying the good compatibility of our framework. Among them, SwinIR-GAN achieves superior perceptual performance on all non-reference metrics across both datasets, while maintaining competitive PSNR and SSIM. This validates the superiority of SwinIR-GAN in balancing fidelity and visual realism for our diffusion SR pipeline, and we thus adopt it as the default pre-upsampling initialization network in our framework.

A.5 More qualitative comparisons

Fig. 6 and Fig. 7 presents more qualitative comparisons of our methods against recent SOTA methods. One can see that our LPNSR achieves comparable or superior visual quality to T2I-utilizing methods such as OSediff [8] and InvSR [4], without relying on any external priors.

A.6 Training and inference algorithms

The pseudo-code of the LPNSR framework training and inference algorithms is summarized in Alg. 1 and 2.

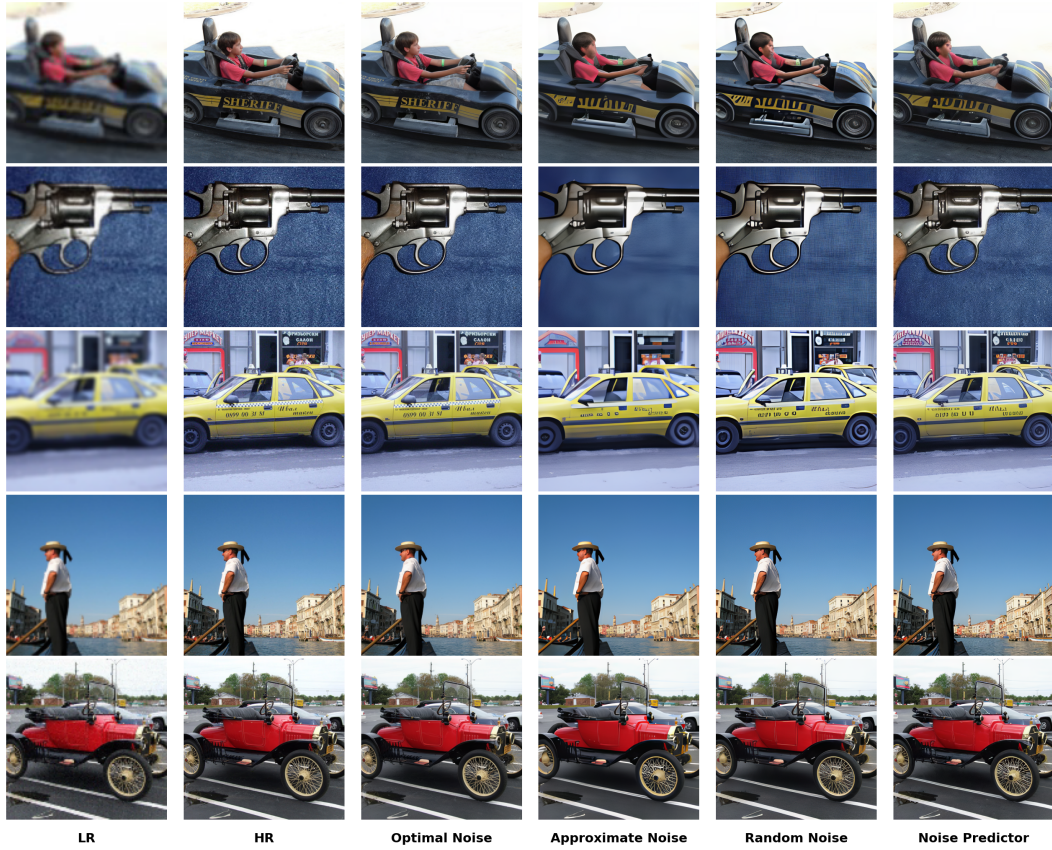


Figure 5: Qualitative comparison of different noise injection strategies. (Zoom in for best view)

Table 7: Quantitative comparison of different pre-upsampling networks for the 4-step diffusion SR on ImageNet-Test and RealSR.

Datasets	Method	PSNR \uparrow	SSIM \uparrow	LPIPS \downarrow	NIQE \downarrow	PI \downarrow	CLIPQA \uparrow	MUSIQ \uparrow
<i>ImageNet-Test</i>	BSRGAN [51]	26.08	0.7052	0.2439	4.4115	3.2022	0.6837	71.7541
	RealESRGAN [48]	26.14	0.7066	0.2411	4.4835	3.2214	0.6774	71.4783
	SwinIR-GAN [45]	26.11	0.7054	0.2424	4.3807	3.1995	0.6921	71.7105
<i>RealSR</i>	BSRGAN [51]	24.66	0.7009	0.3243	4.2239	3.6954	0.7159	67.5517
	RealESRGAN [48]	24.59	0.7001	0.3256	4.2375	3.7023	0.7123	67.4834
	SwinIR-GAN [45]	24.62	0.7003	0.3229	4.2175	3.6963	0.7180	67.5634

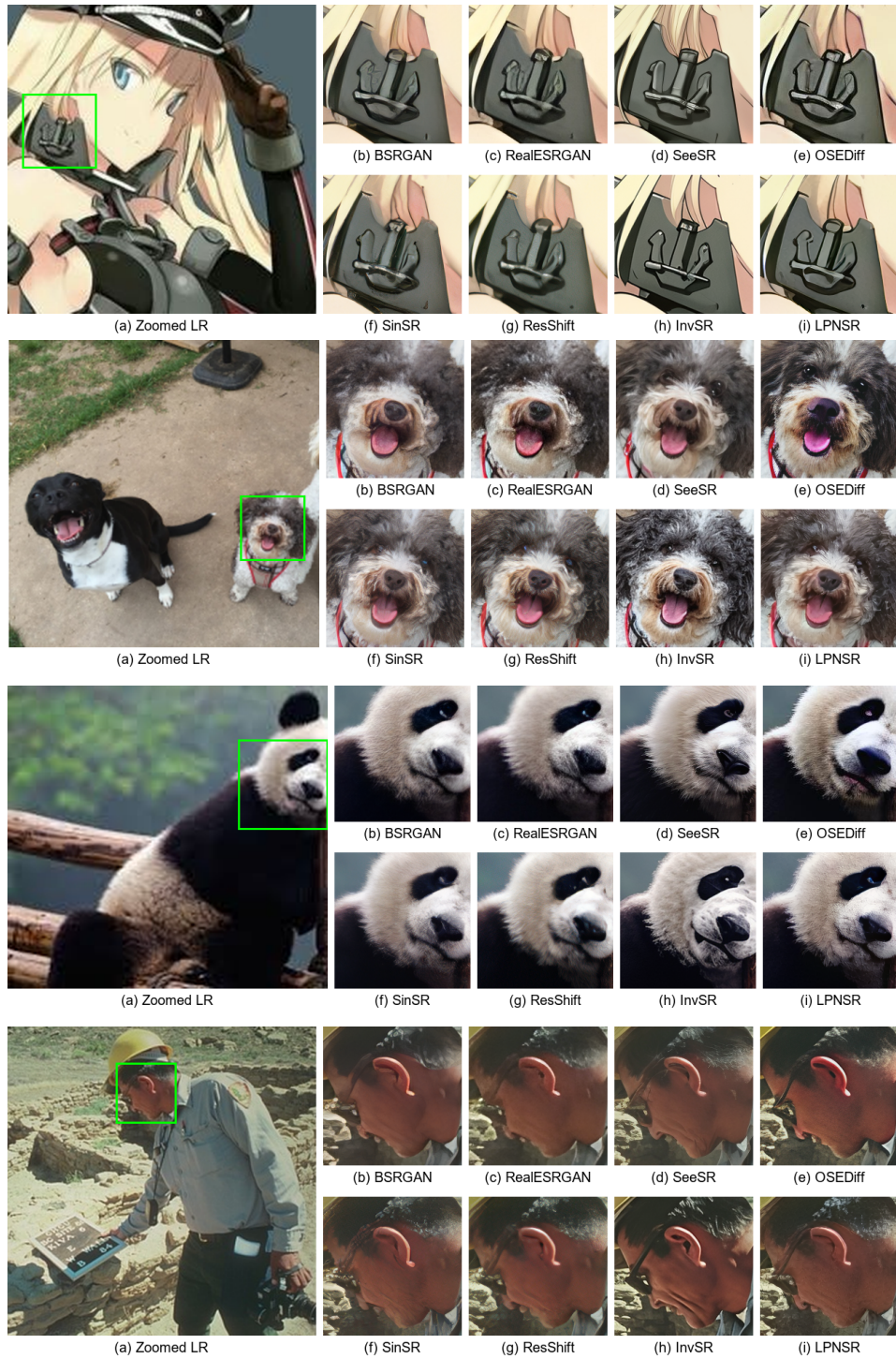


Figure 6: More visualization comparisons of different models. (Zoom in for best view)

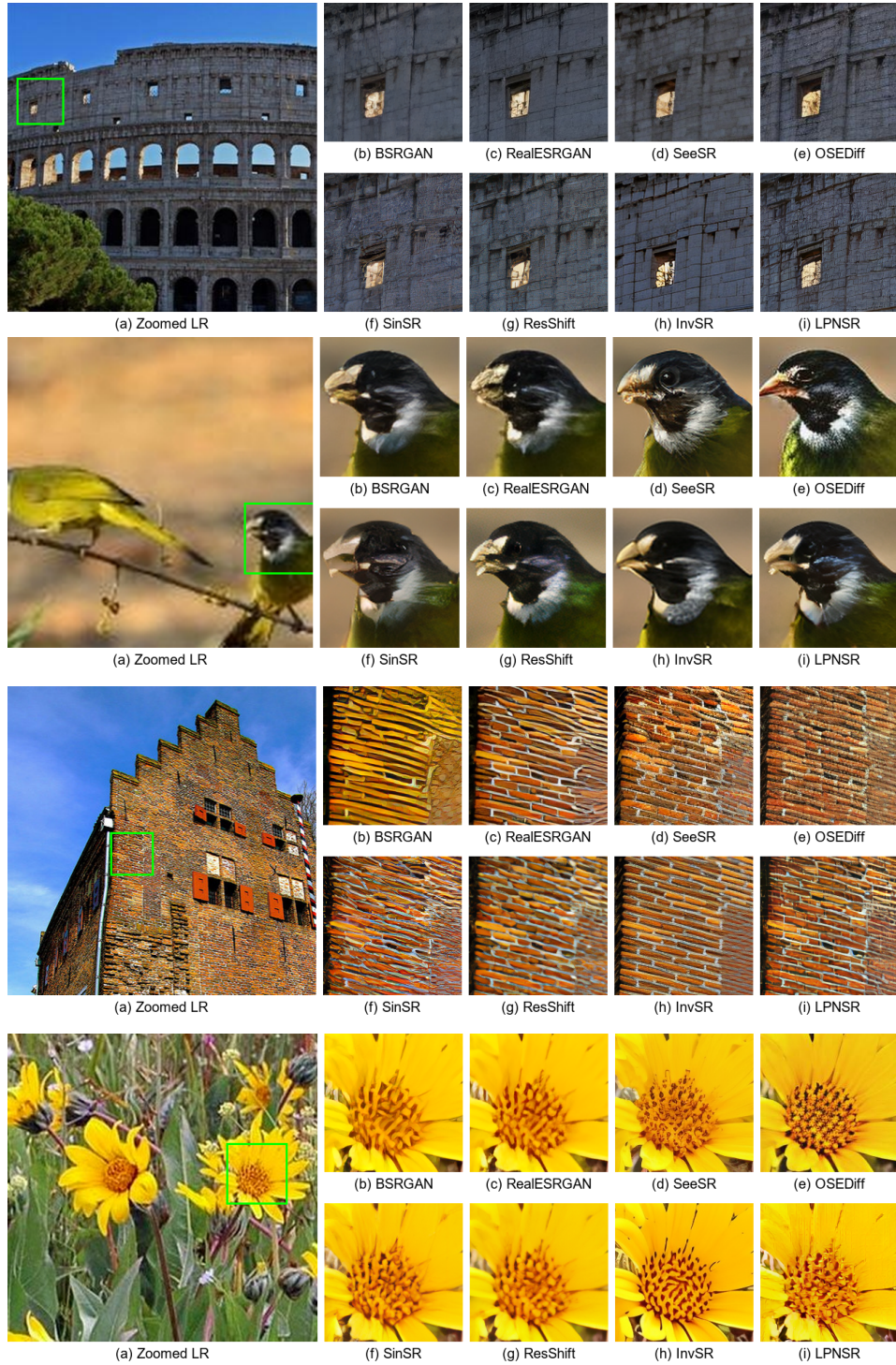


Figure 7: More visualization comparisons of different models. (Zoom in for best view)

Algorithm 1 Noise Predictor Training

Require: HR/LR image pairs \mathcal{D} , pretrained UNet denoiser(frozen), optimizer \mathcal{O} , loss \mathcal{L} ,

Initialize g_w , sampling steps T

Ensure: Trained noise predictor g_w

```
1: while not converged do
2:   Sample  $x_0, y_0 \sim \mathcal{D}$ 
3:   Sample  $z_T \sim \mathcal{N}(0, I)$ ,  $\hat{y}_0 = \text{Bicubic}(y_0)$ 
4:    $x_T = \hat{y}_0 + \kappa\sqrt{\eta_T}z_T$ 
5:   for  $t = T, T-1, \dots, 1$  do
6:     if  $t > 1$  then
7:        $x'_0 = \text{UNet}(x_t, y_0, t)$ 
8:        $\mu = \frac{\eta_{t-1}}{\eta_t}x_t + \frac{\alpha_t}{\eta_t}x'_0$ 
9:        $x_{t-1} = \mu + \sqrt{\Sigma_\theta} \cdot g_w(x_t, x'_0, y_0, t)$ 
10:    else
11:       $x'_0 = \text{UNet}(x_t, y_0, t)$ 
12:    end if
13:  end for
14:  Compute loss  $\mathcal{L}(x'_0, x_0)$ ,  $\mathcal{O}.\text{step}(\mathcal{L})$ 
15: end while
16: return  $g_w$ 
```

Algorithm 2 Inference

Require: LR image y_0 , pretrained UNet denoiser, noise predictor g_w , pretrained SR network, sampling steps T

Ensure: Generated HR image x'_0

```
1: Sample  $z_T \sim \mathcal{N}(0, I)$ ,  $\hat{y}_0 = \text{pre-upsample}(y_0)$ 
2:  $x_T = \hat{y}_0 + \kappa\sqrt{\eta_T}z_T$ 
3: for  $t = T, T-1, \dots, 1$  do
4:   if  $t > 1$  then
5:      $x'_0 = \text{UNet}(x_t, y_0, t)$ 
6:      $\mu = \frac{\eta_{t-1}}{\eta_t}x_t + \frac{\alpha_t}{\eta_t}x'_0$ 
7:      $x_{t-1} = \mu + \sqrt{\Sigma_\theta} \cdot g_w(x_t, x'_0, y_0, t)$ 
8:   else
9:      $x'_0 = \text{UNet}(x_t, y_0, t)$ 
10:  end if
11: end for
12: return  $x'_0$ 
```
